# State Estimation for HALE UAVs with Deep-learning-aided Virtual AOA/SSA Sensors for Analytical Redundancy

Wonkeun Youn[1,*], Hyungtae Lim[2,*], *Student Member, IEEE*, Hyoung Sik Choi[3,†], Matthew B. Rhudy[4], Hyeok Ryu[3], Sungyug Kim[3], and Hyun Myung[2,†], *Senior Member, IEEE*

***Abstract*—High-altitude long-endurance (HALE) unmanned aerial vehicles (UAVs) are employed in a variety of fields because of their ability to fly for a long time at high altitudes, even in the stratosphere. Two paramount concerns exist: enhancing their safety during long-term flight and reducing their weight as much as possible to increase their energy efficiency based on analytical redundancy approaches. In this paper, a novel deep-learning-aided navigation filter is proposed, which consists of two parts: an end-to-end mapping-based synthetic sensor measurement model that utilizes long short-term memory (LSTM) networks to estimate the angle of attack (AOA) and sideslip angle (SSA) and an unscented Kalman filter for state estimation. Our proposed method can not only reduce the weight of HALE UAVs but also ensure their safety by means of an analytical redundancy approach. In contrast to conventional approaches, our LSTM-based method achieves better estimation by virtue of its nonlinear mapping capability.**

***Index Terms*—Sensor Fusion, Aerial Systems: Applications, Field Robotics, AI-Enabled Robotics**

## I. Introduction

AMONG the various types of unmanned aerial vehicles (UAVs), a high-altitude long-endurance (HALE) UAV is an unmanned aircraft capable of performing various missions, such as stratospheric atmospheric weather monitoring, marine pollution monitoring, communications relaying, and forest fire monitoring, while flying in the stratosphere at an altitude of approximately 20 km [1]. In 2016, the Korea Aerospace Research Institute (KARI) developed a HALE electric aerial vehicle known as the EAV-3, as presented in Fig. 1, which can fly powered only by solar energy at a high altitude where the atmosphere is thin and has succeeded in flying in the stratosphere at an altitude of 18.5 km. This record is the third best in the world, after two others achieved in the United States and the United Kingdom [2].

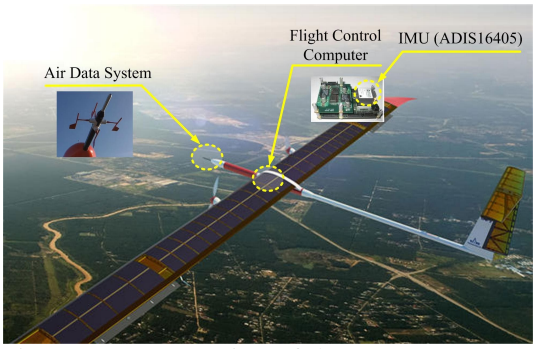

Fig. 1. System overview of the KARI EAV-3 [3].

Considering analytical redundancy, reliability, weight minimization and cost requirements for UAVs, various filtering techniques for the estimation of the angle of attack (AOA) and sideslip angle (SSA) without AOA/SSA vanes have been proposed. In [4], synthetic AOA and SSA measurements were developed based on the aerodynamic parameters of UAVs. In [5], [6], the wind speed triangle equation was used to correlate the airspeed measurement to the ground-speed measurement from the Global Positioning System (GPS) to estimate flow angles without relying on aircraft aerodynamic models. In [7], the AOA and SSA were first estimated in the time domain and then converted into the frequency domain to remove integrated bias and drift.

In addition, in [8], the AOA and SSA were estimated by integrating inertial data over time using optimization algorithms such as the Newton-Raphson solver; however, this method is not suitable for real-time applications due to its computational complexity. In [9], synthetic SSA measurements under the zero-angle assumption were proposed for UAVs without AOA/SSA sensors to improve the state estimation performance during GPS outages, but this approach is applicable only during nonaggressive flight maneuvers. In [10], AOA/SSA estimates could be obtained without GPS measurements if partial aircraft aerodynamic model parameters and an airspeed measurement could be obtained.

In summary, most of the conventional AOA/SSA estimation methods require GPS measurements or sophisticated aircraft dynamic models, which include large numbers of aerodynamic

Manuscript received: December, 17, 2020; Revised February, 5, 2021; Accepted March, 31, 2021.

This paper was recommended for publication by Editor E. Marchand upon evaluation of the Associate Editor and Reviewers' comments. This study was supported by the research project of "Study on the Core Technology of Electric Vertical Take-Off & Landing Aircraft (FR21A07)" funded by Korea Aerospace Research Institute. The student is supported by the BK21 FOUR from the Ministry of Education (Republic of Korea).

†Corresponding authors: Hyoung Sik Choi and Hyun Myung

*Both authors have equally contributed.

[1]Wonkeun Youn is with the Department of Autonomous Vehicle System Engineering, Chungnam National University, Yuseong-gu, Daejeon, 34134, Republic of Korea wkyoun@cnu.ac.kr.

[2]H. Lim and H. Myung are with School of Electrical Engineering, KI-AI, KI-R at KAIST (Korea Advanced Institute of Science and Technology), Daejeon, 34141, South Korea {shapelim, hmyung}@kaist.ac.kr.

[3]Hyoung Sik Choi, Hyeok Ryu, and Sungyug Kim are with the Korea Aerospace Research Institute, Yuseong-gu, Daejeon, 34133, Republic of Korea {chs, hryu, kkisy}@kari.re.kr.

[4]Matthew Rhudy is with the Division of Engineering, Business, and Computing at Pennsylvania State University, Reading, PA 19610, USA mbr5002@psu.edu.

Digital Object Identifier (DOI): see top of this page.

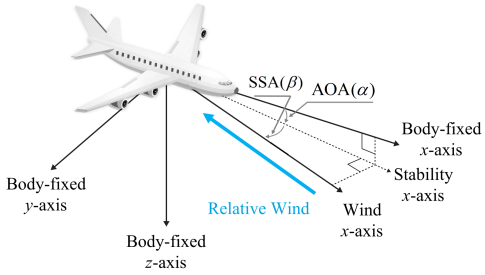


Fig. 2. The relationship between the AOA, SSA, and relative wind.

coefficients. However, obtaining these accurate aerodynamic coefficients requires a series of time-consuming and costly wind tunnel tests or extensive flight testing, and even then, the coefficients may still contain inherent uncertainty. Therefore, the motivation for this work is to propose a novel state estimation approach using deep-learning-aided virtual AOA/SSA sensors that do not require aerodynamic coefficients as an analytical redundancy approach to ensure safety while reducing the weight of a UAV. In particular, long short-term memory (LSTM) networks are employed to accurately model the nonlinear dynamic behavior of sequential AOA/SSA measurements. These synthetic AOA/SSA measurements acquired through the proposed deep-learning-based approach are utilized as the measurements of the navigation filter to estimate the velocity, attitude, inertial measurement unit (IMU) biases, 3D wind states, AOA, and SSA. The proposed algorithm has been comprehensively evaluated using real HALE UAV flight data.

To the best of our knowledge, this paper is the first to introduce a new state estimation algorithm for HALE UAVs with synthetic AOA/SSA measurements based on deep learning. Compared to previous research, the novelty of the proposed algorithm is that it requires neither sophisticated UAV aerodynamics models, which must usually be obtained through time-consuming and cost-inefficient wind tunnel experiments, nor GPS measurements to estimate the AOA/SSA. Instead, the proposed algorithm requires only a minimal set of input parameters, including the acceleration, angular rates, airspeed, and control inputs, which are almost always available for any type of UAV. Thus, the proposed algorithm can be easily implemented for any type of UAV.

## II. Proposed Synthetic AOA/SSA Sensors Based on LSTM Networks

The goal in this section is to derive formulas for synthetic AOA/SSA sensors that require several aerodynamic parameters and then replace these parameters with LSTM networks that do not require them.

### A. Preliminaries

The geometric relationship between the airspeed, AOA, and SSA is depicted in Fig. 2. By utilizing this geometric relationship, the airspeed $\mathbf{v}_a^b$, the AOA $\alpha$, and the SSA $\beta$ can be expressed in the body-fixed frame as follows [11]:

$$\mathbf{v}_{a,k}^b = \begin{bmatrix} u_k \\ v_k \\ w_k \end{bmatrix}_b = \begin{bmatrix} \left|\mathbf{v}_{a,k}^b\right| \cos\alpha_k \cos\beta_k \\ \left|\mathbf{v}_{a,k}^b\right| \sin\beta_k \\ \left|\mathbf{v}_{a,k}^b\right| \sin\alpha_k \cos\beta_k \end{bmatrix} \tag{1}$$

$$\alpha_k = \tan^{-1}\left(\frac{w_k}{u_k}\right) \tag{2}$$

$$\beta_k = \sin^{-1}\left(\frac{v_k}{\left|\mathbf{v}_{a,k}^b\right|}\right) \tag{3}$$

where $u_k$, $v_k$, and $w_k$ denote the $x$, $y$, and $z$ components of the airspeed, respectively. $V_{a,k} = \left|\mathbf{v}_{a,k}^b\right| = \sqrt{u_k^2 + v_k^2 + w_k^2}$ is the magnitude of the airspeed.

### B. Problem Definition

To train LSTM networks to predict the AOA $\alpha_k$ and the SSA $\beta_k$, proper design of the input layers is critical. Thus, this section aims to derive the minimal inputs from an aerodynamic point of view to reduce the complexity of the proposed LSTM networks, which is one of the important academic contributions of this paper. Motivated by our previous research [12], the corresponding inputs for estimating the measured AOA/SSA values from the aerodynamics of the HALE UAV are introduced. Note that in this paper, we use the terms "synthetic AOA/SSA measurements", "synthetic AOA/SSA", and "estimated AOA/SSA" interchangeably.

*1) Synthetic AOA measurement* $\tilde{\alpha}_k$: First, the measured acceleration along the $z$-axis at time $k$ (i.e., $a_{mz,k}$) can be expressed as follows [13]:

$$a_{mz,k} = \frac{1}{M}\xi_k S C_{z,k} \tag{4}$$

where $S$ and $M$ denote the wing area and mass of the HALE UAV, respectively; $\xi_k = \frac{1}{2}\rho V_{a,k}^2$, with $V_{a,k}$ and $\rho$ denoting the airspeed and air density, respectively; and $C_{z,k} = -C_L(\alpha_k)\cos\alpha_k - C_D(\alpha_k)\sin\alpha_k$, with $C_L(\alpha_k)$ and $C_D(\alpha_k)$ denoting the lift and drag coefficients, respectively, with respect to the AOA $\alpha_k$.

Then, $a_{mz,k}$ can be re-expressed as

$$a_{mz,k} = \frac{1}{M}\xi_k S\Big(-C_L(\alpha_k)\cos\alpha_k - C_D(\alpha_k)\sin\alpha_k\Big) \tag{5}$$

Subsequently, the lift coefficient $C_L(\alpha_k)$ in (5) can be formulated as a nonlinear function of $\alpha_k$ as follows [13]:

$$\begin{aligned} C_L(\alpha_k) = {} & (1-\sigma(\alpha_k))\,(C_{L_0} + \alpha_k\, C_{L_\alpha}) \\ & + 2\,\sigma(\alpha_k)\mathrm{sign}(\alpha_k)\sin^2\alpha_k\cos\alpha_k \end{aligned} \tag{6}$$

where $C_{L_0}$ is the constant lift coefficient and $C_{L_\alpha}$ is the linear lift coefficient. In (6), the linear lift relationship described by these aerodynamic coefficients is blended with the effects of stall using a sigmoid function given by

$$\sigma(\alpha_k) = \frac{1 + e^{-L(\alpha_k - \alpha_c)} + e^{L(\alpha_k + \alpha_c)}}{\left(1 + e^{-L(\alpha_k - \alpha_c)}\right)\left(1 + e^{L(\alpha_k + \alpha_c)}\right)} \tag{7}$$

where $\alpha_c$ is the cutoff parameter and $L$ is a positive constant.

The drag coefficient $C_D(\alpha_k)$ in (5) can be similarly represented in terms of $\alpha_k$ with the following nonlinear relationship [13]:

$$C_D(\alpha_k) = C_{D_p} + \frac{(C_{L_0} + \alpha_k\, C_{L_\alpha})^2}{\pi\gamma \mathrm{AR}} \tag{8}$$

where $C_{D_p}$ is the constant drag coefficient from the parasitic drag effect, $\mathrm{AR} = b^2/S$ is the wing aspect ratio, $b$ is the wing

span, and $\gamma$ is the Oswald efficiency factor. The second term in (8) represents the induced drag effect.

The assumption of a small $\alpha_k$ is generally valid, as the flight trajectory of a HALE UAV does not typically include aggressive flight maneuvers with a high AOA $\alpha_k$. Thus, the following approximations of $C_L(\alpha_k)$ and $C_D(\alpha_k)$ in (6) and (8) with a small AOA $\alpha_k$ can be obtained [13]:

$$\begin{aligned} C_L(\alpha_k) &= C_{L_0} + \alpha_k C_{L_\alpha} \\ C_D(\alpha_k) &= C_{D_0} + \alpha_k C_{D_\alpha} \end{aligned} \tag{9}$$

where $C_{D_0}$ and $C_{D_\alpha}$ represent the constant and linear drag coefficients, respectively. For more details on the approximations presented in (9), please refer to [12], [13].

A second-order small-angle approximation for the AOA can be used to replace $\sin\alpha_k$ with $\alpha_k$ and $\cos\alpha_k$ with $1-\alpha_k^2/2$ in (5), resulting in the following expression:

$$\begin{aligned} a_{mz,k} = -\frac{1}{M}\xi_k S\Big(C_{L_0} + \alpha_k(C_{L_\alpha} + C_{D_0}) \\ + \alpha_k^2(C_{D_\alpha} - C_{L_0}/2)\Big) \end{aligned} \tag{10}$$

When designing HALE UAVs, to ensure a long flight duration, small drag forces and large lift forces are greatly desired, resulting in drag coefficients that are much smaller than the lift coefficients. Therefore, the effects of the drag coefficients $C_{D_0}$ and $C_{D_\alpha}$ in (10) can be neglected in this application. Under typical operating conditions, a HALE UAV performs nonaggressive maneuvers, resulting in a small AOA (i.e., $|\alpha_k| \leq 5^\circ$). In addition, the coefficient $C_{L_0}$ is much smaller than $C_{L_\alpha}$; therefore, the quadratic term corresponding to $C_{L_0}$ in (10) can be reasonably neglected, as follows:

$$a_{mz,k} \approx -\frac{1}{M}\xi_k S\left(C_{L_0} + \alpha_k C_{L_\alpha}\right) \tag{11}$$

Rearranging (11) yields

$$\tilde{\alpha}_k \approx -\frac{1}{C_{L_\alpha}}\left(a_{mz,k} + \frac{1}{M}\xi_k S\, C_{L_0}\right) \tag{12}$$

Now, (12) can be used to predict a synthetic AOA using aerodynamic, inertial, and geometric parameters along with the measured z-axis acceleration. However, the corresponding aerodynamic coefficients in (12), such as $C_{L_0}$ and $C_{L_\alpha}$, are assumed to not be available; instead, an LSTM network is trained to capture the nonlinear relationship between the synthetic AOA $\tilde{\alpha}_k$, the dynamic pressure $\xi_k$, and the measured acceleration $a_{mz,k}$.

*2) Synthetic SSA measurement* $\tilde{\beta}_k$: The side force $\mathbf{Y}_k$ can be expressed as

$$\begin{aligned} \mathbf{Y}_k &= m\, a_{my,k} \\ &= \Bigg(c_{Y_0} + c_{Y_\beta}\beta_k + \frac{c_{Y_{\omega_{mx}}}\omega_{mx,k}b}{2V_{a,k}} + \frac{c_{Y_{\omega_{mz}}}\omega_{mz,k}b}{2V_{a,k}} \\ &\quad + c_{Y_{\delta_A}}\delta_{A,k} + c_{Y_{\delta_R}}\delta_{R,k}\Bigg)\xi_k S \end{aligned} \tag{13}$$

where $\delta_{A,k}$ and $\delta_{R,k}$ denote the aileron and rudder control signals, respectively, and $c_{Y_x} \triangleq \frac{\partial c_Y}{\partial x}$, with $c_Y$ denoting the side force coefficient.

Rearranging (13) yields

$$\begin{aligned} \tilde{\beta}_k = \frac{1}{c_{Y_\beta}}\Bigg(\frac{m\, a_{my,k}}{\xi_k S} - c_{Y_0} - \frac{c_{Y_{\omega_{mx}}}\omega_{mx,k}b}{2V_{a,k}} \\ - \frac{c_{Y_{\omega_{mz}}}\omega_{mz,k}b}{2V_{a,k}} - c_{Y_{\delta_A}}\delta_{A,k} - c_{Y_{\delta_R}}\delta_{R,k}\Bigg) \end{aligned} \tag{14}$$

Using (14), the synthetic SSA can be determined using lateral-directional control inputs, angular rate measurements, and the $y$ component of the acceleration. However, this paper assumes that the corresponding aerodynamic coefficients in (14), such as $c_{Y_\beta}$, $c_{Y_0}$, $c_{Y_{\omega_{mx}}}$, $c_{Y_{\omega_{mz}}}$, $c_{Y_\beta}$, $c_{Y_{\delta_A}}$, and $c_{Y_{\delta_R}}$, are not available; instead, an LSTM network is trained to capture the nonlinear relationship between the synthetic SSA $\tilde{\beta}_k$ from (14) and the known variables obtained from the IMU, airspeed sensor, and control input information.

### *C. Proposed LSTM Networks*

Under the assumption that the aerodynamic coefficient parameters in (12) and (14) are not available, LSTM networks are employed to estimate the synthetic AOA $\tilde{\alpha}_k$ and the synthetic SSA $\tilde{\beta}_k$. Let the LSTM network that takes $\mathcal{X}_{\alpha,k}$ as its input and outputs $\tilde{\alpha}_k$ be denoted by $\alpha$-LSTM, and let the other that takes $\mathcal{X}_{\beta,k}$ as its input and estimates $\tilde{\beta}_k$ be denoted by $\beta$-LSTM. LSTM networks take sequential data as their inputs; thus, $\mathcal{X}_{\alpha,k}$ and $\mathcal{X}_{\beta,k}$ are composed of sequential inputs as follows:

$$\mathcal{X}_{\alpha,k} = \mathcal{F}(\{\mathbf{x}_{\alpha,k-T+1}, \mathbf{x}_{\alpha,k-T+2}, \ldots, \mathbf{x}_{\alpha,k}\}) \tag{15}$$

$$\mathcal{X}_{\beta,k} = \mathcal{F}(\{\mathbf{x}_{\beta,k-T+1}, \mathbf{x}_{\beta,k-T+2}, \ldots, \mathbf{x}_{\beta,k}\}) \tag{16}$$

where $T$, $\mathcal{F}(\cdot)$, $\mathbf{x}_{\alpha,k}$, and $\mathbf{x}_{\beta,k}$ denote the sequence length, a normalization function (i.e., a min-max scaler), the input layer of $\alpha$-LSTM at time $k$, and the input layer of $\beta$-LSTM at time $k$, respectively. Accordingly, the outputs of $\alpha$-LSTM ($\mathcal{Y}_{\alpha,k}$) and $\beta$-LSTM ($\mathcal{Y}_{\beta,k}$) are described as follows:

$$\mathcal{Y}_{\alpha,k} = \{\hat{\alpha}_{m,k-T+1}, \hat{\alpha}_{m,k-T+2}, \ldots, \hat{\alpha}_{m,k}\} \tag{17}$$

$$\mathcal{Y}_{\beta,k} = \{\hat{\beta}_{m,k-T+1}, \hat{\beta}_{m,k-T+2}, \ldots, \hat{\beta}_{m,k}\} \tag{18}$$

where $\hat{\alpha}_{m,k}$ and $\hat{\beta}_{m,k}$ represent the output layers of $\alpha$-LSTM and $\beta$-LSTM, respectively. Note that normalized values are acquired from each LSTM network; hence, $\hat{}$ indicates that the corresponding value is normalized. Therefore, $\tilde{\alpha}_k$ and $\tilde{\beta}_k$ must be obtained through denormalization using $\mathcal{F}^{-1}(\cdot)$ as follows:

$$\tilde{\alpha}_k = \mathcal{F}^{-1}(\hat{\alpha}_{m,k}) \tag{19}$$

$$\tilde{\beta}_k = \mathcal{F}^{-1}(\hat{\beta}_{m,k}) \tag{20}$$

From the relationships between the synthetic AOA/SSA and the deployable parameters in (12) and (14), $\mathbf{x}_{\alpha,k}$ and $\mathbf{x}_{\beta,k}$ can be defined as follows:

$$\mathbf{x}_{\alpha,k} = [a_{mz,k}\ \ \xi_k] \in \mathbb{R}^2 \tag{21}$$

$$\mathbf{x}_{\beta,k} = [a_{my,k}\ \ V_{a,k}\ \ \omega_{mx,k}\ \ \omega_{mz,k}\ \ \delta_{A,k}\ \ \delta_{R,k}] \in \mathbb{R}^6 \tag{22}$$

The abovementioned parameters that are employed in (12) and (14) are sufficient to allow the networks to learn the nonlinear relationships of interest. However, the parameters

presented in (21) and (22) are not the only ones affecting the estimation of $\tilde{\alpha}_k$ and $\tilde{\beta}_k$; hence, using only these terms may give rise to information loss. Since many approximations are utilized in the derivation of (12) and (14), including the small AOA assumption and the elimination of negligible parameters and drag coefficients, the other available parameters not given in (12) and (14) may nevertheless have an impact on $\tilde{\alpha}_k$ and $\tilde{\beta}_k$. For that reason, taking all known variables obtained from the IMU, airspeed sensor, and control signals as inputs provides the networks with more high-dimensional information. This may enable the networks to estimate $\tilde{\alpha}_k$ and $\tilde{\beta}_k$ better than they could in the case of taking only a limited number of parameters.

To verify the effectiveness of using all variables, instead of only the input layers $\mathbf{x}_{\alpha,k}$ and $\mathbf{x}_{\beta,k}$ according to (21) and (22) as deduced from the aerodynamic model (i.e., (12) and (14)), all of the available sensor measurements from the IMU, airspeed sensor, and control inputs are utilized as the training inputs for the LSTM networks as follows:

$$\begin{aligned}\mathbf{x'}_{\alpha,k} = [&\omega_{mx,k}\ \omega_{my,k}\ \omega_{mz,k}\ a_{mx,k}\ a_{my,k}\ a_{mz,k}\\ &V_{a,k}\ \delta_{E,k}\ \delta_{A,k}\ \ \delta_{R,k}] \in \mathbb{R}^{10}\end{aligned} \tag{23}$$

$$\begin{aligned}\mathbf{x'}_{\beta,k} = [&\omega_{mx,k}\ \omega_{my,k}\ \omega_{mz,k}\ a_{mx,k}\ a_{my,k}\ a_{mz,k}\\ &V_{a,k}\ \delta_{E,k}\ \delta_{A,k}\ \ \delta_{R,k}] \in \mathbb{R}^{10}\end{aligned} \tag{24}$$

where $\delta_{E,k}$ refers to an elevator control signal and $\boldsymbol{\omega}_{m,k} = (\omega_{mx,k}, \omega_{my,k}, \omega_{mz,k})$ and $\mathbf{a}_{m,k} = (a_{mx,k}, a_{my,k}, a_{mz,k})$ denote the measured angular rates and accelerations, respectively.

For brevity, in the following sections, the minimal input parameters according to (21) and (22) are denoted by `Minimal`, and all sensor information according to (23) and (24) is denoted by `All`. The validity of taking `Minimal` or `All` as the inputs is demonstrated in Section VII.*A*. Note that the aerodynamic parameters in (12) and (14) are not utilized in the proposed LSTM algorithm; instead, they are used only for extracting the minimal input parameters according to (21) and (22), denoted by `LSTM-Minimal`.

### D. Training Loss

In this subsection, the method of training our networks is described. The proposed deep learning architecture is able to estimate $\tilde{\alpha}_k$ and $\tilde{\beta}_k$ by means of optimization. Let $\Theta$ denote the parameters of our network model. Our final goal is to find the optimal parameters $\Theta^*$ for precise estimation based on analytical redundancy by minimizing the $L_2$ loss term, which represents the mean squared error (MSE) between the true value $Y_k$ (i.e., $\alpha$ or $\beta$ as actually measured by AOA/SSA vanes) and the estimated angle value $\hat{Y}_{m,k}$ (i.e., $\hat{\alpha}_{m,k}$ or $\hat{\beta}_{m,k}$), as follows:

$$\Theta^* = \underset{\Theta}{\operatorname{argmin}} \frac{1}{N-T+1} \sum_{k=T-1}^{N} \parallel \mathcal{F}(Y_k) - \hat{Y}_{m,k} \parallel_2 \tag{25}$$

where $N$ denotes the total number of sequences in the training dataset.

## III. State Estimation with Synthetic AOA and SSA Measurements

The aim of nonlinear filtering is to estimate the state vector $\mathbf{x}_k$ from inputs $\mathbf{u}_k$ and measurements $\mathbf{y}_k$ using a recursive Bayesian estimation framework. In this section, the states $\mathbf{x}_k$, inputs $\mathbf{u}_k$, and measurements $\mathbf{y}_k$ are defined. In addition, the state prediction $\mathbf{f}_k$ and the observation function $\mathbf{h}_k$ are defined for the estimation problem.

### A. Problem Formulation

The state vector $\mathbf{x}_k$ and system input vector $\mathbf{u}_k$ can be defined as

$$\begin{cases}\mathbf{x}_k = \begin{bmatrix} u_k & v_k & w_k & \phi_k & \theta_k & \psi_k & \mathbf{a}_{b,k} & \boldsymbol{\omega}_{b,k} & \mathbf{v}^n_{w,k}\end{bmatrix} \in \mathbb{R}^{15}\\ \mathbf{u}_k = [a_{mx,k}\ \ a_{my,k}\ \ a_{mz,k}\ \ \omega_{mx,k}\ \ \omega_{my,k}\ \ \omega_{mz,k}] \in \mathbb{R}^6\end{cases} \tag{26}$$

where $u_k$, $v_k$, and $w_k$ denote the $x$, $y$, and $z$ components of the airspeed, respectively; $\phi_k$, $\theta_k$, and $\psi_k$ denote the roll, pitch, and yaw angles, respectively; $\mathbf{a}_{b,k} = (a_{bx,k}, a_{by,k}, a_{bz,k})$ and $\boldsymbol{\omega}_{b,k} = (\omega_{bx,k}, \omega_{by,k}, \omega_{bz,k})$ are the IMU (accelerometer and gyroscope) biases in the body-fixed frame; and $\mathbf{v}_{w,k} = (\mathbf{v}_{wn,k}, \mathbf{v}_{we,k}, \mathbf{v}_{wd,k})$ is the 3-dimensional wind state of the navigation frame.

### B. State Prediction Equations

The prediction equation related to the body-frame velocities $u_k$, $v_k$, and $w_k$ is given by [14]

$$\begin{aligned}\begin{bmatrix}u_k\\ v_k\\ w_k\end{bmatrix} = &\begin{bmatrix}u_{k-1}\\ v_{k-1}\\ w_{k-1}\end{bmatrix} + T_s \begin{bmatrix}0 & -w_k & v_k\\ w_k & 0 & -u_k\\ -v_k & u_k & 0\end{bmatrix} \left( \begin{bmatrix}\omega_{mx,k}\\ \omega_{my,k}\\ \omega_{mz,k}\end{bmatrix} \right.\\ &\left. - \begin{bmatrix}\omega_{bx,k}\\ \omega_{by,k}\\ \omega_{bz,k}\end{bmatrix} + \boldsymbol{\omega}_{n,k} \right) + (\mathbf{C}^b_n) \begin{bmatrix}0\\ 0\\ \mathrm{g}\end{bmatrix} + \begin{bmatrix}a_{mx,k}\\ a_{my,k}\\ a_{mz,k}\end{bmatrix} - \begin{bmatrix}a_{bx,k}\\ a_{by,k}\\ a_{bz,k}\end{bmatrix}\\ &+ \mathbf{a}_{n,k}\end{aligned} \tag{27}$$

where $\mathrm{g} = 9.80665\,\mathrm{m/s^2}$ is the gravitational acceleration, $T_s$ denotes the sampling time interval, and $\mathbf{C}^b_n$ denotes the direction cosine matrix, which is a rotation matrix that transforms the navigation frame $\{n\}$ into the body-fixed frame $\{b\}$.

The attitude prediction equation can be expressed as

$$\begin{aligned}\begin{bmatrix}\phi_k\\ \theta_k\\ \psi_k\end{bmatrix} = &\begin{bmatrix}\phi_{k-1}\\ \theta_{k-1}\\ \psi_{k-1}\end{bmatrix} + T_s \begin{bmatrix}1 & \sin\phi_k \tan\theta_k & \cos\phi_k \tan\theta_k\\ 0 & \cos\phi_k & -\sin\phi_k\\ 0 & \sin\phi_k \sec\theta_k & \cos\phi_k \sec\theta_k\end{bmatrix}\\ &\cdot \left( \begin{bmatrix}\omega_{mx,k}\\ \omega_{my,k}\\ \omega_{mz,k}\end{bmatrix} - \begin{bmatrix}\omega_{bx,k}\\ \omega_{by,k}\\ \omega_{bz,k}\end{bmatrix} + \boldsymbol{\omega}_{n,k} \right)\end{aligned} \tag{28}$$

For the IMU bias prediction model, a first-order Gaussian Markov (GM) model is used, as follows [11]:

$$\begin{bmatrix}\mathbf{a}_{b,k}\\ \boldsymbol{\omega}_{b,k}\end{bmatrix} = \begin{bmatrix}\mathbf{a}_{b,k-1} \cdot e^{\frac{-T_s}{\tau_a}}\\ \boldsymbol{\omega}_{b,k-1} \cdot e^{\frac{-T_s}{\tau_\omega}}\end{bmatrix} + \begin{bmatrix}\mathbf{w}^a_{k-1}\\ \mathbf{w}^\omega_{k-1}\end{bmatrix} \tag{29}$$

where $\tau_a$ and $\tau_\omega$ denote the correlation times and $\mathbf{w}^a_{k-1}$ and $\mathbf{w}^\omega_{k-1}$ denote the zero-mean WG process noise components for the IMU biases.

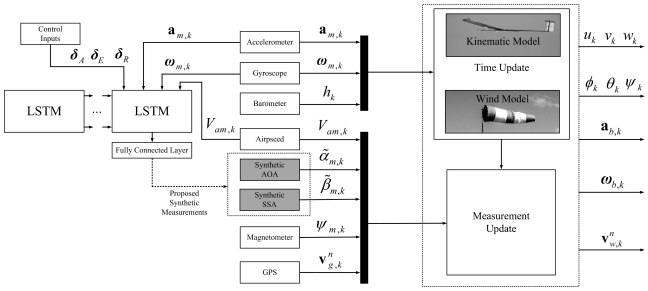


Fig. 3. The proposed deep-learning-aided UKF-based state estimation framework.

TABLE I
UKF parameters

| Symbol | Parameter |
|---|---|
| $\mathbf{R}_{V_m}$ | $1.32 \cdot 10^{-3}$ $(\mathrm{m/s})^2$ |
| $\mathbf{R}_{\alpha_{m,k}}$ | $1.35 \cdot 10^{-5}$ $(\mathrm{rad})^2$ |
| $\mathbf{R}_{\beta_{m,k}}$ | $1.56 \cdot 10^{-5}$ $(\mathrm{rad})^2$ |
| $\mathbf{R}_{\psi_m}$ | $1.43 \cdot 10^{-1}$ $(\mathrm{rad})^2$ |
| $\mathbf{R}_{\mathbf{v}_g^n}$ | $1.45 \cdot 10^{-3}$ $(\mathrm{m/s})^2$ |
| $\mathrm{T}_s$ | 0.1 |
| $\alpha_{\mathrm{ukf}}$ | 0.5 |
| $\beta_{\mathrm{ukf}}$ | 2 |
| $\kappa_{\mathrm{ukf}}$ | 0 |

The discrete process equation for the 3D wind state is assumed to follow an RW process, as follows [11]:

$$\mathbf{v}_{w,k}^n = \mathbf{v}_{w,k-1}^n + \mathbf{w}_{k-1}^v \tag{30}$$

where $\mathbf{w}_{k-1}^v$ refers to the zero-mean Gaussian process noise for the wind velocity [15].

### C. Measurement Equations

In the proposed algorithm, the measurements $\mathbf{y}_k$ at time index $k$ consist of the airspeed $V_{a,k}$, the synthetic AOA $\tilde{\alpha}_k$, the synthetic SSA $\tilde{\beta}_k$, the heading $\psi_k$ (from a magnetometer), and the velocity measurement $\mathbf{v}_{g,k}^n$ (from a GPS receiver), represented as follows:

$$\mathbf{y}_k = [V_{a,k} \quad \overbrace{\tilde{\alpha}_k \quad \tilde{\beta}_k}^{\text{from LSTM}} \quad \psi_k \quad \mathbf{v}_{g,k}^n] \tag{31}$$

Notably, the proposed algorithm does not require AOA and SSA measurements from vanes; instead, $\tilde{\alpha}_k$ and $\tilde{\beta}_k$ in the measurement vector $\mathbf{y}_k$ are the predicted AOA and SSA, respectively, from the proposed LSTM networks. The airspeed, AOA and SSA are defined in terms of the body-frame velocities as shown in (1) - (3), respectively.

The proposed deep-learning-aided navigation filter is illustrated in Fig. 3. In this paper, the unscented Kalman filter (UKF), which does not require Jacobian matrices, is utilized [3]. The details of the UKF are omitted for simplicity. A detailed description of the UKF can be found in [3]

## IV. Experimental Results

### A. Experimental Flight Environment

Flight experiments involving the solar-powered KARI EAV-3 were carried out. Further descriptions of the device equipment, inertial/geometric parameters, and IMU noise characteristics can be found in [3]. The tuning parameters and measurement noise $\mathbf{R}$ for the applied UKF are summarized in Table I.

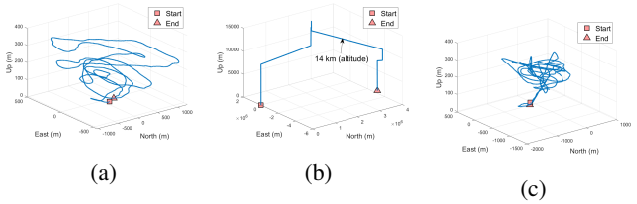


(a) (b) (c)

Fig. 4. Trajectories represented in the datasets.

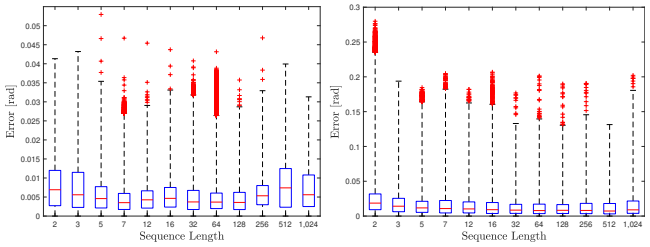


(a) (b)

Fig. 5. Box plots of the (a) AOA ($\alpha$) and (b) SSA ($\beta$) with varying sequence lengths. The sequence lengths were set to 12 for $\alpha$-LSTM and 36 for $\beta$-LSTM.

### B. Acquisition of the Training/Test Data

Synchronized data were collected by an EAV-3 loaded with the aforementioned sensor systems, with a sampling frequency of 10 Hz. Three experiments were conducted, in which the EAV-3 was piloted autonomously with predefined waypoints. Accordingly, all the trajectories are entirely different, as shown in Fig. 4. The individual flight datasets consist of 20,912, 244,082, and 38,807 samples, which correspond to 0.58, 6.78, and 1.07 hours, respectively, when converted into flight time. In particular, the second flight was a long-term flight of approximately 7 hours, during which the HALE UAV reached a maximum altitude of 14 km, enabling the feasibility of the proposed algorithm to be thoroughly verified. After the complete datasets were collected, the second flight dataset (i.e., the longest flight, approximately 7 hours, 244,082 samples) was split into eight sequences, three of which were used as test datasets, i.e., "test dataset 1", "test dataset 2", and "test dataset 3", while the rest were used as the training dataset. Note that the true values of the AOA and SSA were measured from the AOA/SSA vanes.

### C. Training the Networks

After the data were acquired, all of the flight datasets except the aforementioned three test datasets were used to train the networks, including the data from the first and third flights, which are represented in Fig. 4(a) and 4(c), respectively. The proposed networks were trained over 20 epochs using the Adam optimizer [16] with a learning rate of 0.005 and a decay rate of 0.9 per step on an NVidia 2080Ti GPU. Since an overly large batch size or an overly long sequence length will result in overgeneralization, causing the network to tend to be insensitive to unexpected noise attributed to the sensors [17], we set a moderate batch size of 128. The sequence lengths

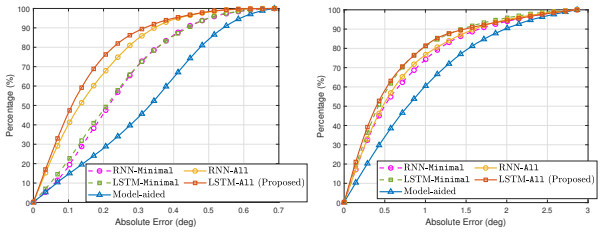


(a) (b)

Fig. 6. CDFs (*a trial that reaches 100% faster is better*) of the (a) AOA ($\alpha$) and (b) SSA ($\beta$).

TABLE II
Comparison with state-of-the-art methods [12], [18] in terms of AOA ($\alpha$) and SSA ($\beta$) performance

| Method | Input type | RMSE (°) | |
|---|---|---|---|
| | | AOA ($\alpha$) | SSA ($\beta$) |
| Model-aided [12] | - | 0.3681 | 7.6742 |
| RNN [18] | `Minimal` | 0.2801 | 1.2543 |
| | `All` | 0.2131 | 1.1164 |
| LSTM (proposed) | `Minimal` | 0.2791 | 1.1339 |
| | `All` | **0.1934** | **1.0926** |

were set to 12 for $\alpha$-`LSTM` and 36 for $\beta$-`LSTM` based on an empirical analysis, as shown in Fig. 5.

## V. Discussion

### A. Impact of Different Input Types

First, the impact of different input types (i.e., `Minimal` and `All`) was investigated. Recurrent neural networks (RNNs) were implemented with `Minimal` and `All` to check the generality of the performance improvement of deep-learning-based approaches, depending on the type of input. In this ablation study, both the RNN and LSTM models with `All` exhibited better cumulative distribution functions (CDFs) and smaller root mean square errors (RMSEs), as represented in Fig. 6 and Table II. In particular, the LSTM networks with `All` yielded the smallest RMSEs for the AOA and SSA estimation.

However, note that the estimation results obtained with `Minimal` (the minimal input parameters necessary to describe the AOA/SSA, as discussed in Section II) were comparable to those obtained with `All` when estimating the SSA. Moreover, little difference in the CDF for the SSA was found when using `Minimal`, as shown in Fig. 6(b). Thus, these results also demonstrate that the minimal input parameters derived from the perspective of aerodynamics are sufficient to estimate the SSA.

### B. Comparison Against the State-of-the-Art Methods

Our best model was compared with the existing state-of-the-art synthetic AOA/SSA estimation method, which is referred to as the model-aided method [12]. The model-aided approach assumes that the aerodynamic coefficient parameters in (12) and (14) are known as a result of wind tunnel experiments, as described in [3]. Comparisons of the results are presented in Figs. 6–8, in which the measured AOA/SSA values are regarded as the ground truth.

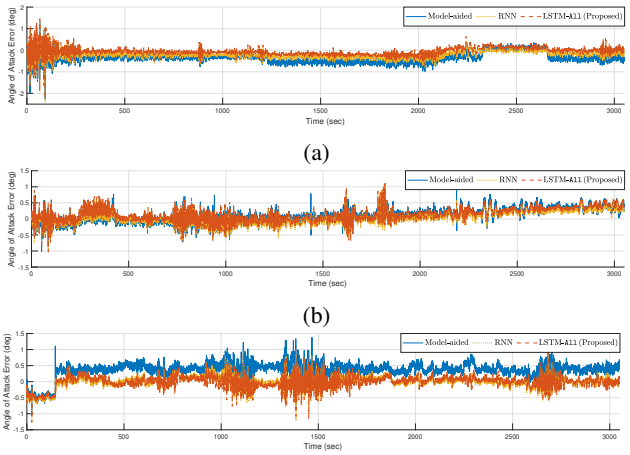


(a)

(b)

(c)

Fig. 7. Comparison of the AOA ($\alpha$) errors on (a) test dataset 1, (b) test dataset 2, and (c) test dataset 3.

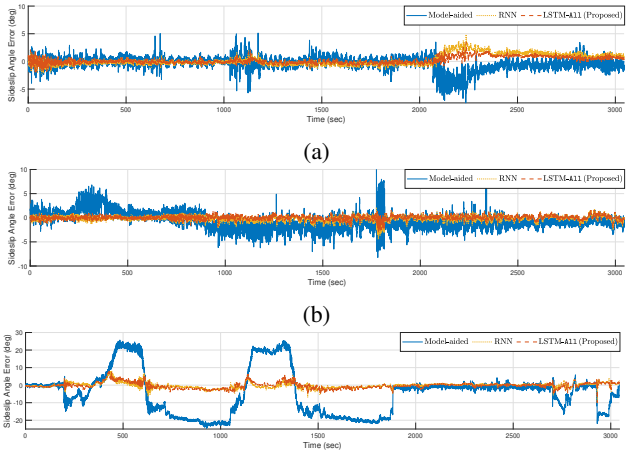


(a)

(b)

(c)

Fig. 8. Comparison of the SSA ($\beta$) errors on (a) test dataset 1, (b) test dataset 2, and (c) test dataset 3.

The LSTM networks with all available information, namely, the LSTM model with `All`, yielded promising estimation results compared to the other methods. Note that the model-aided method produced rather precise AOA and SSA estimates on test dataset 2, as shown in Figs. 7(b) and 8(b), but not on test dataset 3, as shown in Figs. 7(c) and 8(c). Moreover, the model-aided method exhibited excessive overshoot on test dataset 1, as depicted in Fig. 8(a), compared to the learning-based approaches.

There are two primary reasons for these phenomena: a) a growing gap between the real situation and the approximately modeled situation and b) the experimental limitations on the aerodynamic parameters. First, the model-aided approach usually assumes a small AOA or neglects certain constants; in other words, the aerodynamic models are derived under constant-level flight conditions. Thus, they are not accurate for the arbitrary flight maneuvers of a HALE UAV. Second, the aerodynamic parameters, as described in [3], have inherent uncertainties since these values are estimated empirically through wind tunnel testing. In other words, these parameters may reflect undesirable noise. Therefore, using such empirically

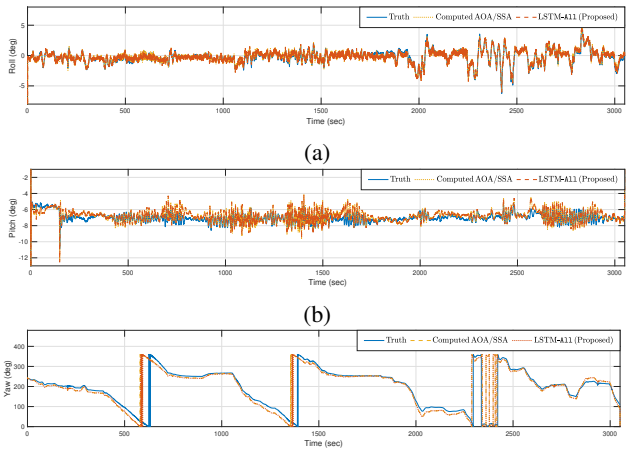


(a) (b) (c)

Fig. 9. Estimation results for the (a) roll, (b) pitch, and (c) yaw on test dataset 3.

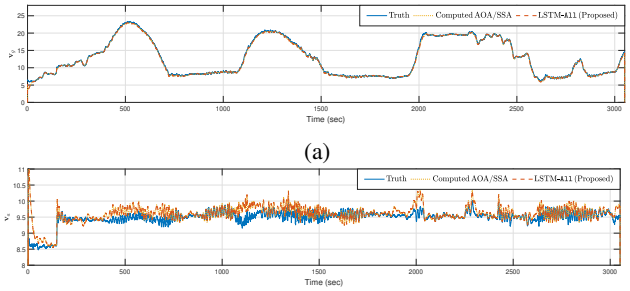


(a) (b)

Fig. 10. Estimation results for the (a) ground speed and (b) airspeed on test dataset 3.

TABLE III
Comparison of attitude estimation performance

| RMSE (°) | Test dataset 1 | | Test dataset 2 | | Test dataset 3 | |
|---|---|---|---|---|---|---|
| | Computed AOA/SSA | **Proposed LSTM** | Computed AOA/SSA | **Proposed LSTM** | Computed AOA/SSA | **Proposed LSTM** |
| Roll | 0.2862 | 0.2849 | 0.7909 | 0.3548 | 0.3373 | 0.3451 |
| Pitch | 0.5491 | 0.5466 | 1.2649 | 0.7313 | 0.4908 | 0.4851 |
| Yaw | 7.2412 | 5.9500 | 14.1907 | 16.5623 | 11.4353 | 13.3018 |

obtained parameters may degrade the accuracy of the state estimation [19].

In contrast to the model-aided method, learning-based approaches can achieve better estimation performance even when the HALE UAV changes altitude significantly since their nonlinear mapping capabilities allow them to learn the general relationship between the sensor data inputs and the AOA/SSA. Figs. 7(c) and 8(c) show that the LSTM-based estimates closely follow the ground truth with little fluctuation. Furthermore, the estimation performance of the RNNs are worse than those of the LSTM networks, implying that the latter have better nonlinear mapping capabilities, which is consistent with the previous literature [20].

Therefore, LSTM-`All` was adopted as the method for predicting the synthetic AOAs and SSAs to be utilized as the measurements in our deep-learning-aided navigation filter.

TABLE IV
Comparison of ADS estimation performance

| RMSE (°) | Test dataset 1 | | Test dataset 2 | | Test dataset 3 | |
|---|---|---|---|---|---|---|
| | Computed AOA/SSA | **Proposed LSTM** | Computed AOA/SSA | **Proposed LSTM** | Computed AOA/SSA | **Proposed LSTM** |
| AOA (°) | 0.1133 | 0.1703 | 0.1204 | 0.2636 | 0.1007 | 0.1170 |
| SSA (°) | 0.1594 | 0.6480 | 0.1540 | 0.5328 | 0.1610 | 1.8403 |

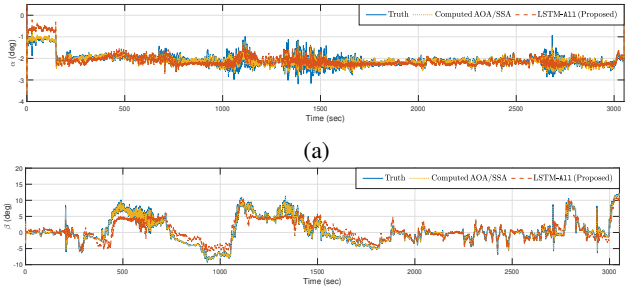


(a) (b)

Fig. 11. Estimation results for the (a) AOA ($\alpha$) and (b) SSA ($\beta$) on test dataset 3.

### *C. Comparison of State Estimation with the Computed AOAs/SSAs*

To demonstrate the validity of the proposed algorithm, the performance of the proposed navigation filter with the predicted AOA/SSA measurements from the LSTM networks, referred to as the "`proposed LSTM`" algorithm, was tested by comparison with the measured AOAs/SSAs from the AOA/SSA vanes, referred to as the "`computed AOA/SSA`" values. For clarity, the `proposed LSTM` and `computed AOA/SSA` measurements can be defined as follows:

$$\begin{cases} \mathbf{y}_k = [V_{a,k} \quad \overbrace{\alpha_{m,k} \;\; \beta_{m,k}}^{\text{from AOA/SSA vane}} \quad \psi_{m,k} \;\; \mathbf{v}^n_{g,k}] \\ \text{for} \quad \texttt{computed AOA/SSA} \\ \mathbf{y}_k = [V_{a,k} \quad \overbrace{\tilde{\alpha}_k \;\; \tilde{\beta}_k}^{\text{from LSTM}} \quad \psi_{m,k} \;\; \mathbf{v}^n_{g,k}] \\ \text{for} \quad \texttt{proposed LSTM} \end{cases} \tag{32}$$

In other words, in the `proposed LSTM`, AOA and SSA measurements are not the real measurements from the AOA/SSA vanes but the synthetic measurements provided by the `proposed LSTM` algorithm. Thus, the measurement noise covariance for these synthetic measurements (i.e., $\mathbf{R}_{\tilde{\alpha}_k}$ and $\mathbf{R}_{\tilde{\beta}_k}$) was set to be approximately 3 times as large as the measurement noise covariance for the real measurements (i.e., $\mathbf{R}_{\alpha_{m,k}}$ and $\mathbf{R}_{\beta_{m,k}}$, as shown in Table I) to mitigate the slight inaccuracy of the synthetic AOA/SSA measurements in the estimation results.

Fig. 9 depicts the roll, pitch, and yaw estimation results based on the `proposed LSTM` and `computed AOA/SSA` measurements, respectively, for comparison with the true values from the GPS/INS system (UAF-C700). The statistical attitude estimation performance of the two algorithms during the flight test is summarized in Table III. In both Fig. 9 and Table III, the attitude estimation results of the `proposed LSTM` algorithm are comparable to those of the `computed AOA/SSA` approach, although the yaw estimation result of

the `proposed LSTM` algorithm is slightly worse than that of the `computed AOA/SSA` approach due to the use of the predicted AOAs/SSAs from the LSTM networks.

Fig. 10(a) depicts the measured and estimated ground speeds during the flight experiment as obtained via the two approaches. Note that the measured ground speed $\mathbf{v}_{g,k}^n$ was obtained from a GPS receiver, while the estimated ground speed was obtained by summing the airspeed estimate and the 3D wind state estimate in the navigation frame on the basis of the wind triangle relationship (i.e., $\hat{\mathbf{v}}_{g,k}^n = \hat{\mathbf{C}}_b^n \hat{\mathbf{v}}_{a,k}^b + \hat{\mathbf{v}}_{w,k}^n$, where $\hat{\mathbf{v}}_{a,k}^b = [\hat{u}_k,\ \hat{v}_k,\ \hat{w}_k]^T$). From this relationship, the accurate attitude $\hat{\mathbf{C}}_b^n$, airspeed $\hat{\mathbf{v}}_{a,k}^b$, and 3D wind state $\hat{\mathbf{v}}_{w,k}^n$ appear to be necessary to obtain the accurate ground speed $\hat{\mathbf{v}}_{g,k}^n$. Fig. 10(a) shows that the estimated ground speeds from the `proposed LSTM` and the `computed AOA/SSA` approaches are both accurate with respect to the measured ground speed from a GPS receiver, thus implying that the estimated attitudes, airspeeds, and 3D wind states obtained with both approaches are accurate.

Similarly, Fig. 10(b) depicts the measured and estimated airspeeds during the flight experiment as obtained via the two approaches. Note that the measured airspeed $\mathbf{v}_{a,k}^n$ was obtained from an airspeed sensor, while the estimated airspeed was obtained in accordance with the relation $V_{a,k} = \sqrt{v_k^2 + u_k^2 + w_k^2}$, representing is the magnitude of the 3-axis velocity in the body frame. Fig. 10(b) shows that both the `proposed LSTM` and `computed AOA/SSA` approaches yield accurate airspeed estimation results, thus implying that the estimated velocities in the body-fixed frame are accurate.

The estimated AOAs and SSAs obtained from the `computed AOA/SSA` and `proposed LSTM` measurements are plotted in Figs. 11(a) and (b), respectively. The statistics concerning the AOA and SSA estimation performance of the two approaches during the flight tests are listed in Table IV, where the measured AOA and SSA values from the air data system (ADS) are considered as the basis for comparison [4]. As seen from Table IV and Fig. 11, the RMSEs of the AOAs and SSAs from the `proposed LSTM` algorithm on the three test datasets are less than approximately $0.27^\circ$ and $1.85^\circ$, respectively. Considering that the estimation performance of the `proposed LSTM` algorithm is comparable to that of the `computed AOA/SSA` approach, the `proposed LSTM` algorithm offers acceptable estimation performance for analytical redundancy.

## VI. Conclusions

This paper has presented a novel deep-learning-aided state estimator for the velocity, attitude, IMU biases, 3D wind state, AOA, and SSA of a HALE UAV. LSTM networks were trained to accurately model the nonlinear dynamics of sequential AOAs/SSAs, and then, the predicted AOA/SSA measurements obtained from the proposed LSTM algorithm were utilized as synthetic measurements in the UKF. The results of long-duration flight experiments demonstrated that the proposed algorithm can yield accurate state estimates for a HALE UAV without real AOA/SSA measurements. Therefore, this study has successfully verified the utility of the proposed algorithm as a concept for achieving analytical redundancy.

## References


[1] O.-J. Kim, S. Yu, H. No, C. Kee, M. Choi, H. Seok, D. Yoon, B. Park, and C. Jee, "Navigation augmentation in urban area by HALE UAV with onboard pseudolite during multi-purpose missions," *Int. J. Aeronaut. Space Sci.*, vol. 18, no. 3, pp. 545–554, 2017.

[2] S.-J. Hwang, S.-G. Kim, C.-W. Kim, and Y.-G. Lee, "Aerodynamic design of the solar-powered high altitude long endurance (HALE) unmanned aerial vehicle (UAV)," *Int. J. Aeronaut. Space Sci.*, vol. 17, no. 1, pp. 132–138, 2016.

[3] W. Youn, H. Choi, A. Cho, S. Kim, and M. B. Rhudy, "Aerodynamic model-aided estimation of attitude, 3D wind, airspeed, AOA, and SSA for high-altitude long-endurance UAV," *IEEE Trans. Aerosp. Electron. Syst.*, vol. 56, no. 6, pp. 4300–4314, 2020.

[4] P. Tian, H. Chao, H. P. Flanagan, S. G. Hagerott, and Y. Gu, "Design and evaluation of UAV flow angle estimation filters," *IEEE Trans. Aerosp. Electron. Syst.*, vol. 55, no. 1, pp. 371–383, 2018.

[5] J. Perry, A. Mohamed, B. Johnson, and R. Lind, "Estimating angle of attack and sideslip under high dynamics on small UAVs," in *Proc. ION GNSS Conference,* 2008, pp. 16–19.

[6] T. A. Johansen, A. Cristofaro, K. Sørensen, J. M. Hansen, and T. I. Fossen, "On estimation of wind velocity, angle-of-attack and sideslip angle of small UAVs using standard sensors," in *Proc. International Conference on Unmanned Aircraft Systems (ICUAS),* 2015, pp. 510–519.

[7] E. A. Morelli, "Real-time aerodynamic parameter estimation without air flow angle measurements," *Journal of Aircraft*, vol. 49, no. 4, pp. 1064–1074, 2012.

[8] C. Ramprasadh and H. Arya, "Multistage-fusion algorithm for estimation of aerodynamic angles in mini aerial vehicle," *Journal of aircraft*, vol. 49, no. 1, pp. 93–100, 2012.

[9] W. Youn, M. B. Rhudy, A. Cho, and H. Myung, "Fuzzy adaptive attitude estimation for a fixed-wing UAV with a virtual SSA sensor during a GPS outage," *IEEE Sens. J.*, vol. 20, no. 3, pp. 1456–1472, 2019.

[10] K. Wise, "Flight testing of the X-45A J-UCAS computational alpha-beta system," in *Proc. AIAA Guidance, Navigation, and Control Conference and Exhibit,* 2006, p. 6215.

[11] M. B. Rhudy, Y. Gu, J. N. Gross, and H. Chao, "Onboard wind velocity estimation comparison for unmanned aircraft systems," *IEEE Trans. Aerosp. Electron. Syst.*, vol. 53, no. 1, pp. 55–66, 2017.

[12] W. Youn, H. S. Choi, H. Ryu, S. Kim, and M. B. Rhudy, "Model-aided state estimation of HALE UAV with synthetic AOA/SSA for analytical redundancy," *IEEE Sens. J.*, vol. 20, no. 14, pp. 7929–7940, 2020.

[13] R. W. Beard and T. W. McLain, *Small Unmanned Aircraft: Theory and Practice*, 1st ed. Princeton university press, 2012.

[14] V. Klein and E. A. Morelli, *Aircraft System Identification: Theory and Practice*, 1st ed. American Institute of Aeronautics and Astronautics Reston, VA, 2006.

[15] M. B. Rhudy, M. L. Fravolini, M. Porcacchia, and M. R. Napolitano, "Comparison of wind speed models within a pitot-free airspeed estimation algorithm using light aviation data," *Aerosp. Sci. Technol.*, vol. 86, pp. 21–29, 2019.

[16] D. Park, Y. Hoshi, and C. C. Kemp, "A multimodal anomaly detector for robot-assisted feeding using an LSTM-based variational autoencoder," *IEEE Robot. Autom. Lett*, vol. 3, no. 3, pp. 1544–1551, 2018.

[17] H. Lim, C. Park, and H. Myung, "RONet: Real-time range-only indoor localization via stacked bidirectional LSTM with residual attention," in *Proc. IEEE/RSJ Int'l Conf. on Intelligent Robots and Systems (IROS),* 2019, pp. 3241–3247.

[18] S. Hochreiter, Y. Bengio, P. Frasconi, and J. Schmidhuber, *A Field Guide to Dynamical Recurrent Neural Networks*, 1st ed. IEEE Press, 2001.

[19] A. Da Ronch, J. Drofelnik, M. P. van Rooij, J. C. Kok, M. Panzeri, and A. Voß, "Aerodynamic and aeroelastic uncertainty quantification of NATO STO AVT-251 unmanned combat aerial vehicle," *Aerosp. Sci. and Technol.*, vol. 91, pp. 627–639, 2019.

[20] A. Ullah, K. Muhammad, J. Del Ser, S. W. Baik, and V. H. C. de Albuquerque, "Activity recognition using temporal optical flow convolutional features and multilayer LSTM," *IEEE Trans. Ind. Electron.*, vol. 66, no. 12, pp. 9692–9702, 2018.